Title

A Study of Position-Sensitive Solid-State Photomultiplier Signal Properties

Permalink

Journal

ISSN

Authors

Schmall, Jeffrey P
Du, Junwei
Judenhofer, Martin S
et al.

Publication Date

DOI

Peer reviewed

A Study of Position-Sensitive Solid-State Photomultiplier Signal Properties

Jeffrey P. Schmall [Student Member, IEEE],
Department of Biomedical Engineering, University of California - Davis, CA, 95616 USA

Junwei Du [Member, IEEE],
Department of Biomedical Engineering, University of California - Davis, CA, 95616 USA

Martin S. Judenhofer [Member, IEEE],
Department of Biomedical Engineering, University of California - Davis, CA, 95616 USA

Purushottam Dokhale,
Radiation Monitoring Devices Inc., Watertown, MA, 02472 USA.

James Christian,
Radiation Monitoring Devices Inc., Watertown, MA, 02472 USA.

Mickel McClish,
Radiation Monitoring Devices Inc., Watertown, MA, 02472 USA.

Kanai S. Shah, and
Radiation Monitoring Devices Inc., Watertown, MA, 02472 USA.

Simon R. Cherry [Fellow, IEEE]
Department of Biomedical Engineering, University of California - Davis, CA, 95616 USA

Abstract

We present an analysis of the signal properties of a position-sensitive solid-state photomultiplier (PS-SSPM) that has an integrated resistive network for position sensing. Attractive features of PS-SSPMs are their large area and ability to resolve small scintillator crystals. However, the large area leads to a high detector capacitance, and in order to achieve high spatial resolution a large network resistor value is required. These inevitably create a low-pass filter that drastically slows what would be a fast micro-cell discharge pulse. Significant changes in the signal shape of the PS-SSPM cathode output as a function of position are observed, which result in a position-dependent time delay when using traditional time pick-off methods such as leading edge discrimination and constant fraction discrimination. The timing resolution and time delay, as a function of position, were characterized for two different PS-SSPM designs, a continuous 10 mm × 10 mm PS-SSPM and a tiled 2 × 2 array of 5 mm × 5 mm PS-SSPMs. After time delay correction, the block timing resolution, measured with a 6 × 6 array of $1.3 \times 1.3 \times 20$ mm^3 LSO crystals, was 8.6 ns and 8.5 ns, with the 10 mm PS-SSPM and 5 mm PS-SSPM respectively. The effect of crystal size on timing resolution was also studied, and contrary to expectation, a small improvement was measured when reducing the crystal size from 1.3 mm to 0.5 mm. Digital timing methods were studied and

(srcherry@ucdavis.edu)..

showed great promise for allowing accurate timing by implementation of a leading edge time pick-off. Position-dependent changes in signal shape on the anode side also are present, which complicates peak height data acquisition methods used for positioning. We studied the effect of trigger position on signal amplitude, flood histogram quality, and depth-of-interaction resolution in a dual-ended readout detector configuration. We conclude that detector timing and positioning can be significantly improved by implementation of digital timing methods and by accounting for changes in the shape of the signals from PS-SSPMs.

Keywords

Positron emission tomography; solid-state photomultipliers; silicon photomultipliers; G-APDs; depth-of-interaction; small animal imaging

I. Introduction

For improved image spatial resolution to be realized in small animal positron emission tomography (PET), localization of annihilation photons must be improved during detection [1]. Two promising strategies to improve localization of events are the use of direct conversion materials, for example semiconductors such as CdZnTe, with finely spaced electrodes [2]-[5], or scintillation-based detectors, where the scintillator has sub-millimeter pixelization [6]-[9]. For finely pixelated scintillator arrays it is difficult to know whether the dominant cause of mispositioning is due to inter-crystal Compton scatter, statistical limits imposed by the production and collection of scintillator light, or the spatial resolution of the photodetector. Here we present results from a novel position-sensitive photodetector, shown to have micron level spatial resolution [10], which we use in conjunction with LSO arrays with crystal sizes of 0.5 and 1.3 mm.

Silicon photomultipliers (SiPMs) are an attractive photodetector for replacement of traditional vacuum tube photomultipliers when depth-of-interaction (DOI) estimation and magnetic field compatibility are needed [11]. Such measurements require that the detectors must be very compact for simultaneous PET and magnetic resonance imaging and also highly transparent to 511 keV photons when using a dual-ended readout for DOI estimation. Several position-sensitive SiPM designs have been proposed and evaluated [12], [13]. To date, none of these designs have shown the ability to decode scintillation arrays <0.5 mm and also the size of an individual SiPM element is typically limited to $\sim 3 \times 3$ mm^2 in area.

In collaboration with Radiation Monitoring Devices, Inc. (Watertown, MA) we have been investigating a CMOS SiPM, designed and optimized for maximum spatial resolution, which we refer to as the position-sensitive solid-state photomultiplier (PS-SSPM). Table I summarizes the device parameters. In this design the output of each micro-cell is connected to an array of micro-patterned network resistors to multiplex the channel count and encode the weighted average position information by the ratio of signal energies at the four corner anode contacts (see Fig. 1). A common cathode signal is used for timing and triggering the data acquisition system.

Designing a large area and high spatial resolution PS-SSPM is a difficult task due to the inherent trade-offs. Capacitance and dark count rate are proportional to the active area and high spatial resolution requires the use of a large network resistor value. High capacitance and high resistance create a RC low-pass filter that results in undesirable signal properties that include: low amplitude, slow rise time, noisy signals, and a pulse shape that varies with position across the device. These effects inherently limit the timing performance, count rate capability, and cause complications for peak height data acquisition methods. However, scintillation detectors with excellent spatial resolution can be constructed using this approach. The goal of this study is to characterize the trade-off between spatial resolution and pulse shape properties for two different size PS-SSPMs and explore the use of data correction methods that may provide a pathway towards achieving improved timing performance while maintaining excellent identification of small scintillator crystal elements.

Much of this work follows, and in some cases builds upon, our knowledge of position-sensitive avalanche photodiode (PS-APD) signal properties [14], [15]. As we will show, PS-SSPMs share the cathode signal position dependent timing shift found in PS-APD designs but with the addition of a significant position-dependent rise time shift in the four corner anode signals following a charge sensitive preamplifier. In our previous publication on PS-SSPMs [16] we optimized detector operating conditions (applied bias and temperature) by using a signal to noise analysis. Here we present a detailed characterization of the position-dependent time response of the PS-SSPM cathode signal for two PS-SSPM sizes, a 10 mm × 10 mm PS-SSPM and a 5 mm × 5 mm PS-SSPM. The position-dependent variation in anode signal shape is shown for a 5 mm × 5 mm PS-SSPM coupled to a high spatial resolution scintillation array; its effect on data acquisition was analyzed by measurements of flood quality and depth of interaction resolution. For clarity, a list of the studies that were performed is presented in Table II.

II. Materials and Methods

A. Device Readout and Signal Shape Characterization

Detectors were biased at their optimal bias voltages of 31 V for the 10 mm PS-SSPM and 30.5 V for the 5 mm PS-SSPM array, determined from previous studies [16], using an Agilent N6700B power supply. For both detectors the same readout scheme was used, shown in Fig. 2, where the cathode channel was fed directly into an Ortec 579 fast filter amplifier and the four corner anode channels were amplified by Cremat CR-113 preamplifiers before further amplification and shaping with a CAEN n568B spectroscopy amplifier (shaping time 100 ns). The setup for time stamp generation was similar to the publication of Wu 2009 [14], using an Ortec 584 for constant fraction (CF) or leading edge (LE) time pick off and an Ortec 416A gate and delay generator to adjust the trigger delay for the digitization using a simultaneously sampled DAQ board (UEI, Inc., Walpole, MA) [17]. For full pulse digitization of the raw detector signals a 2.4 GHz bandwidth oscilloscope (Tectronics, DPO 7254) with 40 Gs/sec sampling rate was used. All measurements were performed with the detector and preamplifiers inside of an aluminum enclosure. Temperature was controlled using an Air-Jet Crystal Cooler (FTS Systems, Inc., Stone Ridge, NY) and monitored with a DigiSense Type K thermocouple attached to the backside

of the PS-SSPM. All measurements were made at 0° C, unless specifically noted. A 2.22 MBq ^{22}Na point source was used for all measurements.

B. PS-SSPM Timing Resolution Measurements

The reference detector used to measure the PS-SSPM timing properties was composed of a polished LSO block ($13 \times 13 \times 20$ mm^3) coupled to a single channel Hamamatsu R6231 PMT biased at −900V. The timing signal from the PMT signals was generated by a CF with a delay line of 3 ns. A Tennelec TC 863 time to amplitude converter (TAC) was used to measure the time difference between the generated time stamps. Tests with two reference detectors in coincidence showed a timing resolution of 1.6 ns. Thus, the degradation in the measured PS-SSPM timing resolution due to the timing resolution of the LSO PMT reference detector is negligible. In all measurements the PMT signal was used as the start signal of the TAC and the PS-SSPM signal as the stop signal.

Flood histograms were generated using Anger equations:

$$x = \frac{(A+B) - (C+D)}{A+B+C+D} \qquad y = \frac{(A+D) - (C+B)}{A+B+C+D} \quad (1)$$

A look up table (LUT) for separating individual crystals was used to study the positional dependence of the PS-SSPM time response. The LUT was generated by an automatic flood segmentation algorithm and then adjusted manually [18]. A timing spectrum for each crystal was generated and a Gaussian fit was applied to measure the timing resolution (FWHM) and time shift (peak position).

1) Characterization of 10 mm PS-SSPM and 5 mm PS-SSPM timing properties

—A 6×6 array of polished $1.3 \times 1.3 \times 20$ mm^3 crystals separated by ESR reflector (3M, St. Paul, MN) (total array size $8.2 \times 8.2 \times 20$ mm^3) was used to compare the measured time delay between different positions on the PS-SSPM surface and also to characterize the timing resolution as a function of position. These measurements were performed for both the 10 mm PS-SSPM and a single 5 mm PS-SSPM from the 2×2 array. Initial experiments were aimed at optimizing the time pick-off method for PS-SSPMs. Timing spectra using CF and LE discrimination were generated, with delays of 40 ns, 50 ns, and 60 ns for the CF circuit and at LE thresholds of 125 keV (3 mV), 185 keV (4 mV), and 250 keV (5 mV). In order not to confuse the lower energy threshold (energy discrimination) and leading edge threshold (timing discrimination), all lower energy thresholds will be presented in keV and leading edge thresholds in mV. A threshold of 125 keV corresponds to a raw signal amplitude of ~3 mV (before any signal amplification) and is close to the noise floor for both the 5 mm PS-SSPM and 10 mm PS-SSPM. Timing spectra with an increased lower energy threshold were created by post processing of the data. The whole array timing resolution measurements were calculated after correcting for the time shift of individual crystals by first aligning all crystal timing spectra.

2) Timing resolution of 0.5 mm LYSO array coupled to a 5 mm PS-SSPM—The

high spatial resolution scintillation array is composed of 13×13 unpolished LYSO crystals with individual sizes of $0.5 \times 0.5 \times 20$ mm^3 (total array size $8 \times 8 \times 20$ mm^3). Timing

resolution with the 0.5 mm scintillation array was only studied for the 5 mm PS-SSPM, as these smaller crystals could not be resolved using the 10 mm PS-SSPM.

The array was designed to be readout from both ends for DOI estimation and uses a 50 μm thick Toray paper diffuse reflector. For timing measurements, only one end of the array was read out by a single 5 mm PS-SSPM, the far end of the scintillation array was covered with Teflon reflector. The scintillation array was positioned such that the surface of a single 5 mm × 5 mm PS-SSPM was entirely covered by the scintillation array. This resulted in 8×7, of the 13×13, crystals being coupled and resolvable by the PS-SSPM. Again a LUT was derived from flood images and applied to the coincidence timing data for crystal segmentation and a lower energy threshold of 250 keV was set in post processing.

C. Digital Timing Methods

A coincidence setup consisting of two 5 mm PS-SSPMs, separated by 8 cm and each having a single $1 \times 1 \times 20$ mm^3 LSO crystal coupled to the center of the detector, was used to generate signals for investigating the timing resolution using digital timing methods. The cathode signals of each detector were split using a Phillips Scientific 744 fan in/out unit with one branch fed directly into the oscilloscope with 50 ohm termination and the other branch to the previously described setup for analog discrimination; a 250 keV lower energy threshold was set during post processing. Each digitized signal contained 35k values sampled every 25 ps for a total duration of 875 ns. The raw data was then imported into MATLAB (The Mathworks, Natick, MA) for further processing; 2000 signals were saved as the coincidence data set. Signals were linearly interpolated.

Timing resolution measured by digital CF methods was found to be similar to hardware CF discrimination (data not shown). First the effects of timing resolution as a function LE threshold level were studied. Subsequently a walk correction was developed and implemented. Lastly the effect of sampling rate on digital timing was studied. The sampling rate was downsampled from the originally acquired 40 Gs/sec data to 5 Gs/sec, 500 Ms/sec, and 100 Ms/sec.

D. Position Dependence of Anode Signals

To visualize the shift in anode rise time a single $1 \times 1 \times 20$ mm^3 LSO crystal wrapped in Teflon was coupled to the corner of a single 5 mm PS-SSPM. The fast oscilloscope digitized the four corner anode signal waveforms simultaneously after being amplified by Cremat CR-113 charge sensitive preamplifiers and also after shaping using the Caen N568B spectroscopy amplifier.

As described in the beginning of Section A, and also in [15], the data acquisition system is based on digitizing the peak amplitude after shaping. Because of the PS-SSPM's anode signal position dependent shape we observed changes in flood histogram dynamic range and energy estimation by varying the delay between the CF generated time stamp and acquisition trigger time (which we refer to as the DAQ trigger delay). To study this effect in more detail, the setup from Section B.2 was used (0.5 mm LYSO array, PMT PS-SSPM coincidence geometry) except the LSO block coupled to the PMT was replaced with a $1 \times 20 \times 20$ mm^2 polished LSO slab. This enables the ^{22}Na source to be collimated into a fan

beam traversing the LSO block perpendicularly approximately 2 mm above the PS-SSPM surface allowing for the best possible flood histogram quality. The Ortec 416A gate and delay generator was used to step the DAQ trigger delay in intervals of 100 ns. Flood histograms were generated using Anger type equations (Eq. 1). Signal amplitude was estimated by the position of the 511 keV photopeak and flood quality was calculated by an average peak to valley ratio from a horizontal line profile through the center of the flood histogram.

E. Depth-Encoding using 5 mm PS-SSPMs and Dual-Ended Readout

A 10×10 array of $0.7 \times 0.7 \times 20$ mm^3 crystals, each with unpolished surfaces and separated by a specular reflector (3M, St Paul, MN, ESR) for optimal DOI response [7], was read out at both ends with 5 mm PS-SSPMs. The same electronic collimation described in Section D was used; with the PMT placed on a linear stage to adjust the irradiation depth along the 20 mm long array. The ^{22}Na source was placed centrally between both detectors with a source to detector distance of 6 cm. The ^{22}Na source size was estimated to be ~0.5 mm FWHM by microCT. No correction for the source size or beam geometry was made. Combined flood histograms were created by averaging the X and Y event positions measured by each PS-SSPM using:

$$x = \frac{x_1 + x_2}{2}, \quad y = \frac{y_1 + y_2}{2}, \quad (2)$$

The DOI position was estimated by the ratio of the detected energy (sum of four anode channels) from the top PS-SSPM to the combined energies of the top (E_1) and bottom (E_2) PS-SSPMs:

$$DOI_{response} = \frac{E_1}{E_1 + E_2} \quad (3)$$

The electronics setup for DOI measurement and calibration were similar to previously described methods [7]. Measurements were made at nine depths at 2 mm intervals and 200k events were recorded per position. The DOI resolution measurement was performed at two DAQ trigger delays, –300 ns relative to summed signal peak and at the summed signal peak (see Fig. 12 for clarification of trigger delay). Energy was scaled such that a 250 keV energy lower energy threshold was used for both trigger delays. The DOI resolution was calculated as the FWHM of a Gaussian fit to the data.

A flood histogram quality metric, k, was calculated at each DAQ trigger delay using:

$$k = \frac{1}{j} \sum_1^j \frac{|d_i - d_{i+1}|}{\left(\frac{w_{i,x} + w_{i,y}}{2} + \frac{w_{i+1,x} + w_{i+1,y}}{2} \right)} \quad (4)$$

where w_i and d_i are the width (FWHM, averaged over x and y projections) and crystal separation distance respectively of the ith crystal in the flood histogram using j number of crystal pairs. A more detailed discussion of flood histogram quality evaluation can be found in Yang et al [19] and also Lau et al [20]. It is expected that improvements in this metric

would translate to improved intrinsic spatial resolution of the detector. Flood quality metrics for the two DAQ trigger delays were compared on combined flood histograms recorded in singles mode with 5 million counts.

III. Results

A. Device Readout and Signal Shape Characterization

Using a single $2 \times 2 \times 10$ mm^3 LSO crystal wrapped in Teflon coupled to the device center the cathode channel rise time (10% to 90%) and signal amplitude was characterized for both the 5 mm PS-SSPM and 10 mm PS-SSPM. Using 1000 digitized pulses from each detector, the rise time was measured to be 101 ± 14 ns and 93 ± 9 ns for the 5 mm PS-SSPM and 10 mm PS-SSPM respectively (Fig. 3). The slow signal rise time is a consequence of the high detector capacitance and integrated resistive network. PS-SSPM capacitance, for both designs, was estimated as the number of micro-cells multiplied by the capacitance per cell (in Table I). This is not exact, as the micro-cells are connected in a grid, making the parallel and series capacitance calculation very difficult, however it does provide an upper bound. It is also expected that there is a very large parasitic capacitance component increasing the total device capacitance. The cathode channel signal amplitude, for both the 5 mm and 10 mm PS-SSPM, is ~10 mV for a 511 keV interaction.

B. PS-SSPM Timing Resolution

1) Characterization of 10 mm PS-SSPM and 5 mm PS-SSPM timing properties

—Fig. 4 shows the raw timing spectrum of the 1.3 mm LSO array coupled to the 10 mm PS-SSPM. The raw timing spectra with the 5 mm PS-SSPM and 1.3 mm LSO array show similar dispersion and asymmetry. As can be seen in Fig. 5 and Fig. 6, the timing properties of the 10 mm and 5 mm PS-SSPM are very similar in the position dependence of the time delay and timing resolution. For the 10 mm PS-SSPM, signals from the corner crystals arrive earlier and have a time delay of ~72 ns with respect to the start signal with a timing resolution of 6.9 ns (best); center crystal signals arrive later with a time delay of ~92 ns and a timing resolution of ~11.6 ns (worst). For the 5 mm PS-SSPM, corner crystals have a time delay of ~68 ns and a timing resolution of ~6.7 ns (best); center crystals have a time delay of ~92 ns and a timing resolution of ~13.1 ns (worst). After correcting for the crystal specific time delays, the timing resolution was recalculated using the data from all crystals – the results are given in Table III. The reproducibility of these measurements (assuming the array isn't removed and recoupled) is estimated to be < 0.1 ns.

There was an improvement in timing resolution for the 10 mm PS-SSPM at 0° C compared to 20° C. This trend was not as pronounced in measurements with the 5 mm PS-SSPM and can be attributed to the higher noise of the 10 mm PS-SSPM. There was no measureable difference in timing resolution using different CF delays of 40, 50 and 60 ns with either the 5 mm or 10 mm PS-SSPM. For the 5 mm PS-SSPM, timing was slightly improved when using a lower leading edge threshold, which is expected. This trend was not found with the 10 mm PS-SSPM, as at a leading edge level of 3 mV both signal and noise will generate a time stamp demonstrating that LE timing with the 10 mm PS-SSPM is very susceptible to noise.

Fig. 7 shows timing data from a crystal coupled to the corner of the 5 mm PS-SSPM at two different lower energy thresholds. CF and LE timing resolution with both the 5 mm PS-SSPM and 10 mm PS-SSPM improved when increasing the lower energy threshold from 250 keV to 450 keV.

2) Timing resolution of 0.5 mm LYSO array coupled to a 5 mm PS-SSPM—Fig. 8 shows the crystal segmented timing data generated with the 5 mm PS-SSPM and 0.5 mm LYSO array. After time shift correction, the global timing resolution measured with the 0.5 mm LYSO array was 8.7 ns, using a lower energy threshold of 250 keV. This result is better than the timing resolution of 12.0 ns obtained with the 1.3 mm array. A direct comparison of data from an individual crystal in the 1.3 mm and 0.5 mm arrays is shown in Fig. 9. The light output of the 0.5 mm LYSO array is expected to be lower than the 1.3 mm LSO array because of the unpolished crystal surface and diffuse reflector used. However, there also will be a greater variability in the time shift within the area covered by a single 1.3 mm crystal compared with a single 0.5 mm crystal – we refer to this as an intracrystal time shift. This data suggests that intracrystal time shifts are present when using larger cross-section crystal dimensions.

C. Digital Timing Methods

Fig. 10 shows the dependence of the timing resolution on the threshold in a digital leading edge discriminator. An improvement of 7.5 ns was measured when lowering the LE threshold from 1.5 mV to 0.5 mV (Fig. 10). This 1 mV difference represents a 10% drop of the leading edge threshold because of the low amplitude signals (~10 mV amplitude for a 511 keV event). It should be noted that the coincidence is generated by a hardware LE threshold at ~3 mV. A hardware LE at ~0.5 mV would not be practical as this would mainly generate a time stamp on noise pulses and therefore can only be implemented in post processing of the data.

A walk correction for PS-SSPM signals was also developed and improved timing resolution for the 1.5 mV LE threshold from 14.9 ns to 10.1 ns. The effect of time walk correction when using lower LE thresholds was less apparent; timing resolution was improved by 0.3 ns and 0.1 ns for digital LE thresholds of 1.0 mV and 0.5 mV, respectively. The digital timing resolution values quoted are from a crystal positioned on the center of the device surface. The data was measured with two PS-SSPMs in coincidence. To compare with the previous measurements that were obtained with a PS-SSPM in coincidence with a PMT (which reflects an individual PS-SSPM detector measurement) the calculated individual detector timing resolution using digital timing methods at a LE threshold of 0.5 mV was 5.2 ns at the device center with a lower energy threshold of 250 keV.

To study the effect of sampling rate on timing resolution, the coincidence data set was downsampled to as low as 100 Ms/sec. The coincidence timing resolution with digital LE of 0.5 mV at 100 Ms/sec was 7.5 ns (compared to 7.4 ns at the original sampling rate), showing no significant degradation in timing resolution by downsampling the acquired data, implying that widely used free running ADCs can be used.

D. Positional Dependence of Anode Signals

Fig. 11 shows there is a significant change in signal shape between the four corner anode signals when the PS-SSPM is illuminated off center. This is due to the very high, and positionally dependent, RC time constant. This is a problem for data acquisition schemes that capture the peak heights of several shaped signals using a common trigger source. As shown here for the PS-SSPM (Fig. 11), the peaks of the four anode signals do not line up in time and no single time delay can be chosen. The measured time delay of the summed signal peak, however, is not position sensitive, and does not change as the illumination position on the detector surface is changed; the summed signal peak is used here as a temporal reference (see Fig. 12). Flood histograms derived from a common trigger (from the fast cathode signal) are shown in Fig. 13 for seven different trigger delays. The other triggers are arranged to occur at a fraction of the summed signal peak, with each change corresponding to roughly 100 ns in time. As the trigger point, with respect to the peak of the summed signal, is changed from –400 ns to +200 ns the appearance of the flood histogram changes dramatically. In particular, the dynamic range decreases with increasing trigger delay. From any other position-sensitive photodetector one would not expect this result; using Anger logic and sampling a shaped signal peak height, the flood should be smaller when the trigger delay is set before the signal's peak amplitude, reach a maximum size when sampled at the signal's peak amplitude and then again shrink when past the peak. The best flood quality (here defined as an average peak to valley ratio) is reached when the trigger is –300 ns from signal peak, however this condition does not result in largest measured signal amplitude (measured at signal peak). Because the scintillation array used in this experiment was optimized for DOI resolution, energy resolution was not quantified. Instead, to better understand the effect of digitizing at lower signal amplitudes, DOI response and resolution was measured.

E. 5 mm PS-SSPM Dual Ended Readout of 0.7 mm Depth of Interaction Scintillation Array

Combined flood histograms from the two PS-SSPMs at either end of the scintillator array, obtained from triggers at -300 ns and summed signal peak, also showed differences in dynamic range (Fig. 14). However, it is not so straightforward to determine which flood histogram is superior in terms of crystal identification. Before applying Equation 4 to the two flood histograms, the data was rebinned such that the array dimensions in pixels were matched. This ensured that differences in crystal identification were not due to the bin size chosen for histogramming. The average flood histogram quality metric, measured over all 6 × 6 crystals in the array, was 2.63 and 2.38 for the –300 ns trigger and signal peak trigger flood, respectively. The improvement was most pronounced in the corner and edge crystals, resulting in a 28% improvement for the –300 ns trigger flood. This may lead to higher intrinsic detector spatial resolution. Flood quality for the center crystals in the array was similar, however this is not surprising as the central crystals are very well resolved independent of trigger delay.

Fig. 15 shows the DOI measured response for both the –300 ns delay trigger (top) and signal peak (bottom) trigger. The DOI response was very linear, as indicated in Fig. 16. The calculated DOI resolution for center and corner crystals is shown in Fig. 17. Crystals in the corner of the array are most affected by changes in data acquisition settings. As expected,

the FWHM of the DOI response was better at all depths when sampling the shaped anode signals at the summed signal peak. The average DOI resolution, for all crystals at all depths, was 3.14 mm sampling using the trigger delay set to signal peak and 3.76 mm sampling at a trigger delay of –300 ns from the combined signal peak height.

IV. Discussion

PS-SSPMs are being explored as a possible technology for small-animal PET and PET/MRI. The goal of this work was to explore the potential of PS-SSPMs, with close attention to timing properties given that timing been identified as the major limitation of this photodetector.

The PS-SSPM timing results, from both the 10 mm PS-SSPM and 5 mm PS-SSPM designs studied in this work, share many similarities with timing results obtained with PS-APDs [14], [15]. The timing shift across the surface of the PS-SSPM sensing area is of similar magnitude to that measured with PS-APDs, though it is important to note the device area; in terms of distance from center to corner the 5 mm PS-SSPM has a shift of 7.1 ns/mm, the 10 mm PS-SSPM a shift of 2.9 ns/mm, and a 14 mm PS-APD for comparison has a shift of 2.5 ns/mm. For the 5 mm PS-SSPM, the large time shift per unit distance is not limited to time shifts between crystals at different positions on the detector surface. As the crystal cross section is increased the coupled micro-cells will have wider differences in their RC constant, resulting in a significant intracrystal time shift. This is a major degrading factor for timing resolution with the 5 mm PS-SSPM when using larger crystals, and provides an improved individual crystal timing resolution when using very small crystal sizes even though the light output is typically lower.

Another similarity between PS-SSPMs and PS-APDs is the dependence of timing resolution on position; for both the 10 mm PS-SSPM and 5 mm PS-SSPM timing resolution is better at the corner of the device than at the center. A major distinction between PS-SSPMs and PS-APDs is need for a preamplifier on the cathode channel. The raw PS-APD signal cannot be visualized unless a preamplifier is used (in our PS-APD setup we use a Cremat CR-110). The PS-SSPM readout used has no preamplifier on the cathode channel. If a charge sensitive preamplifier (CR-113) is used the rise time increases from 100 ns to over 500 ns. We are exploring other preamplifier concepts, which have been investigated by other groups [21], [22], to improve the PS-SSPM's cathode channel timing response. Though the timing properties of PS-SSPMs are only slightly worse than PS-APDs and should be acceptable for most small animal imaging applications.

For most small-animal imaging applications a wide-open energy window (250 keV – 750 keV) is often used, meaning that the detector performance at low energy thresholds must be accounted for. We thus wanted to optimize the time response of the 5 mm PS-SSPM using low energy thresholds (250 keV) and digital timing techniques have produced the best results (coincidence timing resolution of 7.4 ns). To compare with other analog timing measurements, using NIM electronics to readout a $1 \times 1 \times 20$ mm^3 LSO crystal coupled to the center of a 5 mm PS-SSPM, a timing resolution of 9.4 ns was reported in [10]. In our experience noise seems to be the limiting factor in obtaining good timing resolution. As

shown in Fig. 10, a very low leading edge threshold provides the best timing resolution measurement. The challenge with this approach is that a discriminator this close to the noise floor typically cannot be implement in hardware. Application of such a low leading edge threshold is only feasible in post processing, after coincidence events have been acquired based on a higher threshold applied to the shaped energy signals.

The change in flood histogram dynamic range with trigger delay is caused by the observation that PS-SSPM anode signals do not have a constant rise time and are dependent upon position. This effect is not observed for PS-APDs. For a data acquisition system that use a common trigger to digitize the peak of the four position outputs, PS-SSPM results depend on the trigger delay and the crystal location. We showed that the quality of the flood histogram (assessed using Eq. 4) and the DOI resolution were optimized at different trigger delays, thus they cannot both be optimized simultaneously. This is a trade-off that is easily fixed if a full signal digitization DAQ system is used as two digitization points could be kept. Since the rise time is also proportional to the signal position we will investigate if a measured signal rise time could be incorporated into a modified Anger equation to further improve crystal identification.

Moving to a free running ADC sampling DAQ system PS-SSPM signals are fairly advantageous because of their shape, compared to other photodetector signal properties. As it was shown, a 100 MHz sampling rate would be sufficient to achieve the maximum intrinsic timing performance. The high anode channel count of the 5 mm PS-SSPM array could also be mitigated if a front-end readout incorporated a FPGA for calculation of the Anger position or other readout methods, such as pulse width modulation [23].

V. Conclusion

We have characterized the pulse shape and timing performance of PS-SSPMs. The overall conclusion of our work is that using the signal correction techniques discussed in this paper with PS-SSPMs a timing resolution adequate for most small animal PET applications can be obtained. Compared to PS-APDs, PS-SSPMs achieve adequate timing performance at room temperature while PSAPDs typically need to be cooled to $0°$ C. If a compact, magnetic field compatible, detector is needed to readout finely pixelated crystal arrays PS-SSPMs provide an interesting alternative.

Acknowledgments

References

1. Stickel JR, Cherry SR. High-resolution PET detector design: Modeling components of intrinsic spatial resolution. Phys. Med. Biol. Jan.2005 50:179–195. [PubMed: 15742938]

2. Drezet A, Monnet O, Mathy F, Montemont G, Verger L. CdZnTe detectors for small field of view positron emission tomographic imaging. Nucl. Inst. Meth. A. Feb.2007 571:465–470.

3. Ishii K, Kikuchi Y, Matsuyama S, Kanai Y, Kotani K, Ito T, Yamazaki H, Funaki Y, Iwata R, Itoh M, Yanai K, Hatazawa J, Itoh N, Tanizaki N, Amano D, Yamada M, Yamaguchi T. First

achievement of less than 1 mm FWHM resolution in practical semiconductor animal PET scanner. Nucl. Inst. Meth. A. Jun.2007 576:435–440.

4. Gu Y, Matteson JL, Skelton RT, Deal AC, Stephan EA, Duttweiler F, Gasaway TM, Levin CS. Study of high-resolution 3D cadmium zinc telluride detector for PET. Phys. Med. Biol. Feb.2011 56:1563–1584. [PubMed: 21335649]

5. Mitchell GS, Sinha S, Stickel JR, Bowen SL, Cirignano LJ, Dokhale P, Kim H, Shah KS, Cherry SR. CdTe Strip Detector Characterization for High Resolution Small Animal PET. IEEE Trans. Nucl. Sci. Jun.2008 55:870–876.

6. Stickel JR, Qi J, Cherry SR. Fabrication and Characterization of a 0.5 mm Lutetium Oxyorthosilicate Detector Array for High-Resolution PET Applications. J. Nucl. Med. Jan.2007 48:115–121. [PubMed: 17204707]

7. James SS, Yang Y, Wu Y, Farrell R, Dokhale P, Shah KS, Cherry SR. Experimental Characterization and system simulations of depth of interaction PET detectors using 0.5 mm and 0.7 mm LSO arrays. Phys. Med. Biol. Jun.2009 54:4605–4619. [PubMed: 19567945]

8. Song TY, Wu H, Komarov S, Siegel SB, Tai Y. A sub-millimeter resolution PET detector module using a multi-pixel photon counter array. Phys. Med. Biol. Apr.2010 55:2573–2587. [PubMed: 20393236]

9. Yamamoto S, Watabe H, Hatazawa J. Performance comparison of Si-PM based block detectors with different pixel sizes for an ultrahigh-resolution small-animal PET system. Phys. Med. Biol. Sep. 2011 56:N227–N236. [PubMed: 21937773]

10. McClish M, Dokhale P, Christian J, Staples C, Johnson E, Augustine F, Shah KS. Performance measurements from LYSO scintillators coupled to a CMOS position sensitive SSPM detector. Nucl. Inst. and Meth. in Phys. Res. A. Oct.2011 652:264–267.

11. Roncali E, Cherry SR. Application of silicon photomultipliers to positron emission tomography. Ann. Biomed. Eng. Apr.2011 39:1358–1377. [PubMed: 21321792]

12. Schultz V, Berker Y, Berneking A, Omidvari N, Kiessling F, Gola A, Piemonte C. Sensitivity encoded silicon photomultiplier--a new sensor for high-resolution PET-MRI. Phys. Med. Biol. Jun.2013 58:4733–4748. [PubMed: 23782507]

13. Fischer P, Piemonte C. Interpolating silicon photomultipliers. Nucl. Inst. Meth. A. Nov.2012 718:320–322.

14. Wu Y, Ng TSC, Yang Y, Shah KS, Farrell R, Cherry SR. A study of the timing properties of position-sensitive avalanche photodiodes. Phys. Med. Biol. Aug.2009 54:5155–5172. [PubMed: 19671971]

15. Reynolds PD, Olcott PD, Pratx G, Lau FWY, Levin CS. Convex Optimization of Coincidence Time Resolution for a High-Resolution PET System. IEEE Trans. Med. Imaging. Feb.2011 30:391–400. [PubMed: 20876008]

16. Schmall JP, Du J, Yang Y, Dokhale PA, McClish M, Christian J, Shah KS, Cherry SR. Comparison of large-area position-sensitive solid-state photomultipliers for small animal PET. Phys. Med. Biol. Nov.2012 57:8119–8134. [PubMed: 23172720]

17. Judenhofer MS, Pichler BJ, Cherry SR. Evaluation of high performance data acquisition boards for simultaneous sampling of fast signals from PET detectors. Phys. Med. Biol. Dec.2004 50:29–44. [PubMed: 15715420]

18. Chaudhari AJ, Joshi AA, Bowen SL, Leahy RM, Cherry SR, Badawi RD. Crystal identification in positron emission tomography using nonrigid registration to a Fourier-based template. Phys. Med. Biol. Aug.2008 53:5011–5027. [PubMed: 18723924]

19. Yang Y, Wu Y, Farrell R, Dokhale P, Shah KS, Cherry SR. Signal and noise properties of position-sensitive avalanche photodiodes. Phys. Med. Biol. Sep.2011 56:6327–6336. [PubMed: 21896961]

20. Lau FWY, Vandenbroucke A, Reynolds P, Ho H, Innes D, Levin CS. Signal Conditioning Technique for Position Sensitive Photodetectors to Manipulate Pixelated Crystal Identification Capabilities. IEEE Trans. Nucl. Sci. Sep.2012 59:1815–1822.

21. Huizenga J, Seifert S, Schreuder F, van Dam HT, Dendooven P, Lohner H, Vinke R, Schaart DR. A fast peramplifer concept for SiPM-based time-of-flight PET detectors. Nucl. Inst. Meth. A. Dec. 2012 695:379–384.

22. Seifert S, Schaart DR, van Dam VT, Huizenga J, Ruud V, Dendooven P, Lohner H, Beekman FJ.
    A high bandwidth preamplifier for SiPM-based TOF PET scintillation detectors. IEEE Nuc. Sci.
    Symp. Conf. Rec. 2008:1616–1619.

23. Bieniosek MF, Olcutt PD, Levin CS. Compact pulse width modulation circuitry for silicon
    photomultiplier readout. Phys. Med. Biol. Jul.2013 58:5049–5059. [PubMed: 23831601]
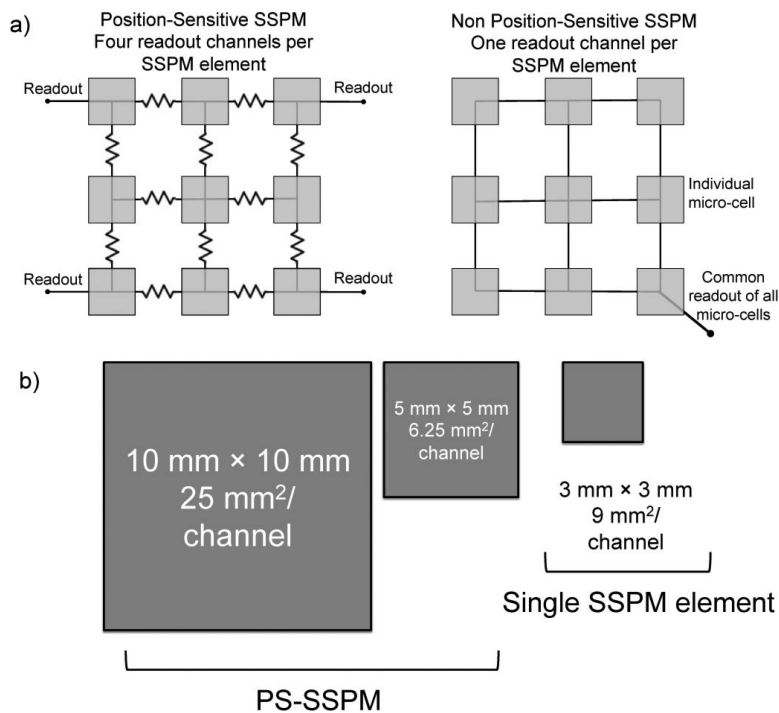
Fig. 1.
a) Example of a 3×3 micro-cell SSPM design; position-sensitive (left) and non position-sensitive (right) SSPM configuration. b) Illustration of area per channel count for different SSPM designs compared with a typical single element SiPM.
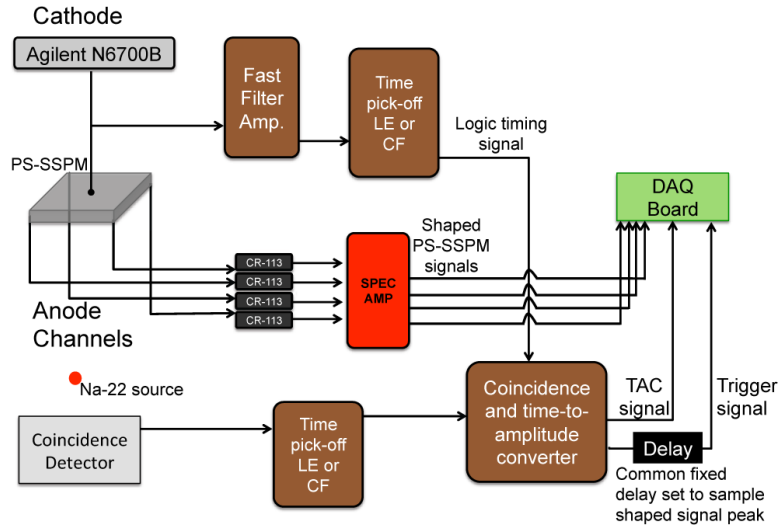
Fig. 2.
Experimental signal readout schematic. For timing resolution measurements of the 5 mm and 10 mm PS-SSPM the coincidence/reference detector is a single channel PMT. For digital timing resolution measurements two 5 mm PS-SSPMs are used in coincidence. For DOI measurements two 5 mm PS-SSPMs are used to read out the array at both ends and the 8 anode channel are digitized.
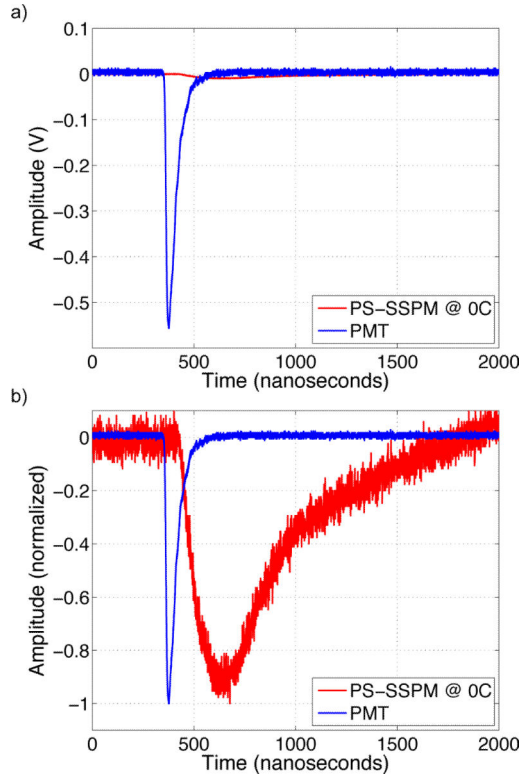
Fig. 3.
Raw cathode signal waveform (no preamplifier) of a 5 mm × 5 mm PS-SSPM. The PS-SSPM signal amplitude for a 511 keV interaction is ~10 mV and the average signal rise time (10%- 90%) is 101 ns ± 14 ns. PMT signal is shown for comparison. (a) Comparison of the raw signal amplitudes and (b) signal amplitudes are normalized to maximum amplitude.
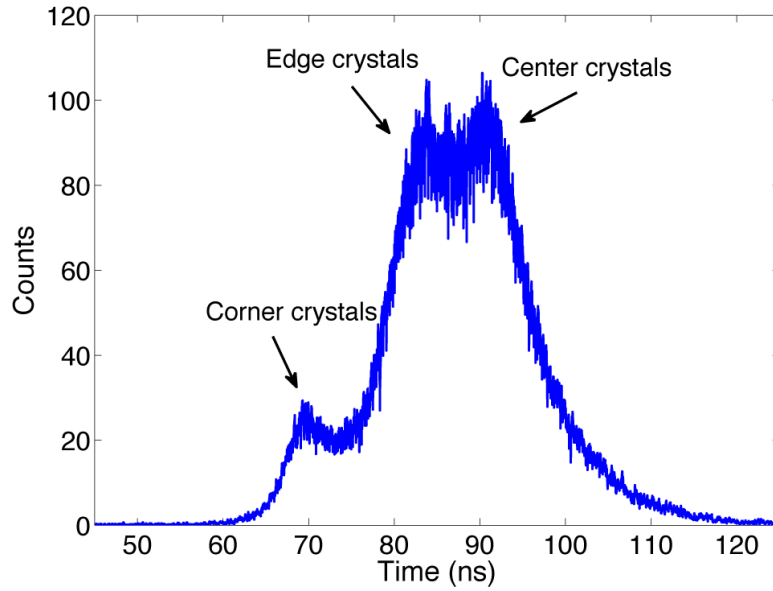
Fig. 4.
Raw timing spectra generated with PMT (start) and 10 mm PS-SSPM (stop) coincidence setup. The 1.3 mm LSO array was coupled to the 10 mm PS-SSPM and no crystal segmentation timing correction applied. A similar result is obtained with the 5 mm PS-SSPM.
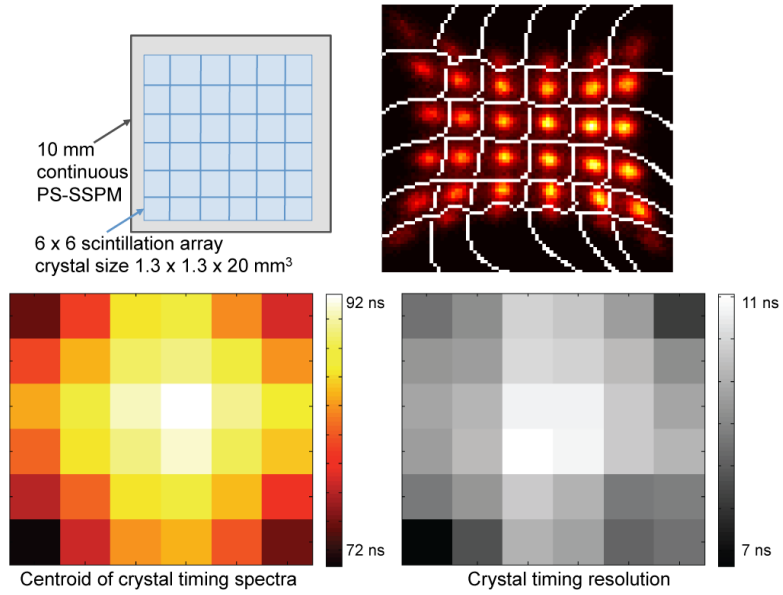
Fig. 5.
Per crystal timing results from the 10 mm PS-SSPM coupled to the 1.3 mm LSO array. Using the flood LUT (top right) a timing spectrum for each crystal in the array was generated; Timing data was generated using CF with a delay of 60 ns. The detector was cooled to 0°C and a global lower energy threshold of 250 keV was applied. After crystal time shift correction, the global block timing resolution was 10.4 ns.
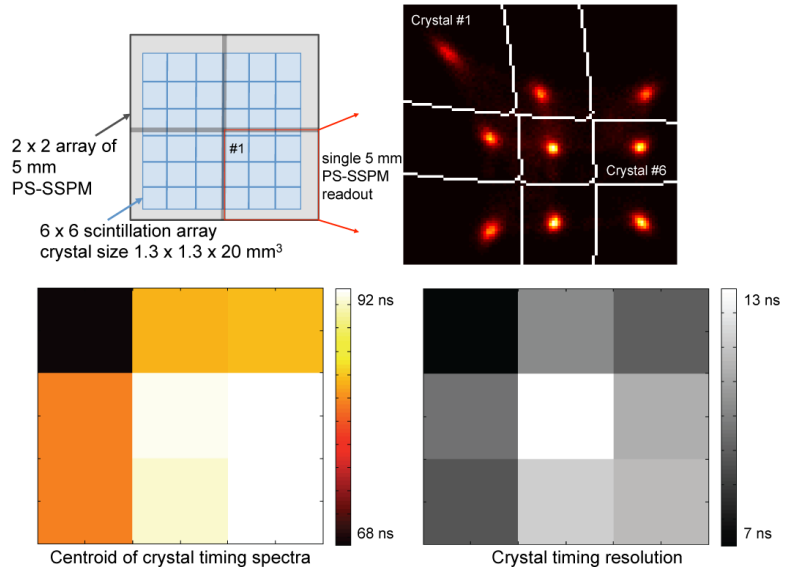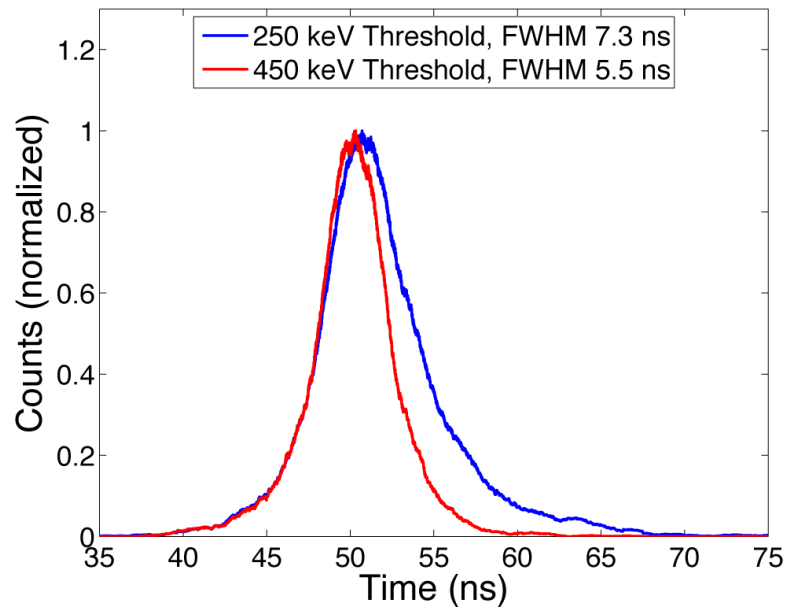
Fig. 6.
Per crystal timing results from the 5 mm PS-SSPM coupled to the 1.3 mm LSO array. Due to the similarity of the response from each 5 mm PS-SSPM in the 2×2 array, results for only one 5 mm PS-SSPM are shown. Timing data was generated using CF with a delay of 60 ns. The detector was cooled to $0°$ C and a global lower energy threshold of 250 keV was applied. After crystal time shift correction, the global block timing resolution was 12.1 ns.

Fig. 7.
Effect of lower energy threshold on the timing resolution with the 5 mm PS-SSPM. Data is from a crystal in the 1.3 mm LSO array coupled to the corner of the device (crystal #1 see Fig. 6). Timing spectrum was generated using CF with a 40 ns delay.
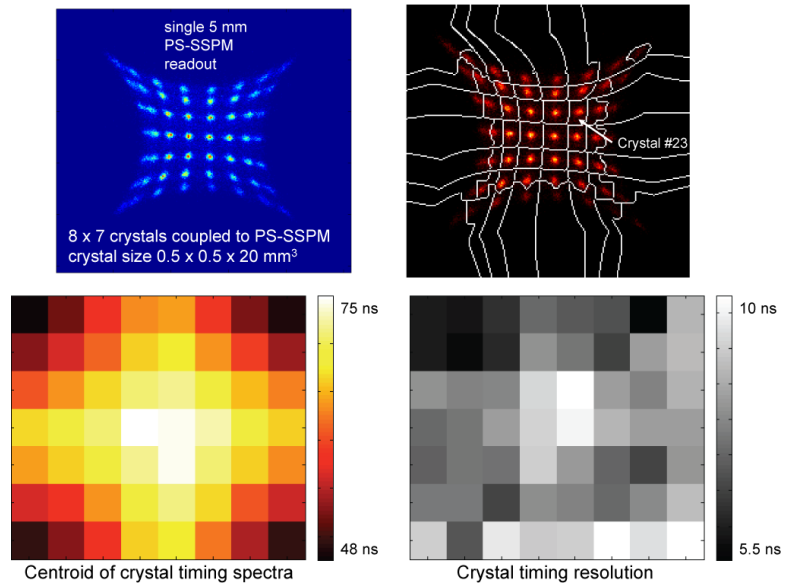
Fig. 8.
Per crystal timing results with the 0.5 mm LYSO array coupled to a 5 mm PS-SSPM. Timing data was generated using CF with a delay of 40 ns. The detector was cooled to 0°C and a global lower energy threshold of 250 keV was applied. After crystal time shift correction, the global block timing resolution was 8.7 ns.
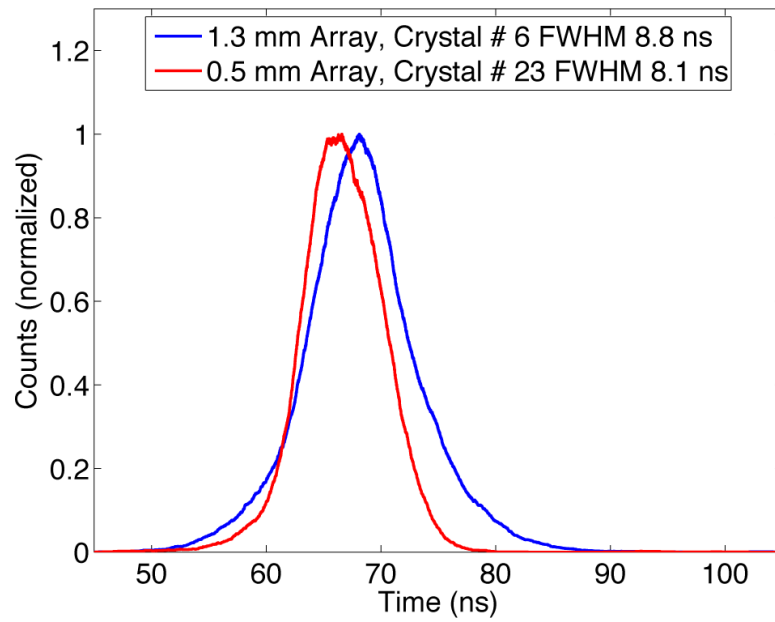
Fig. 9.
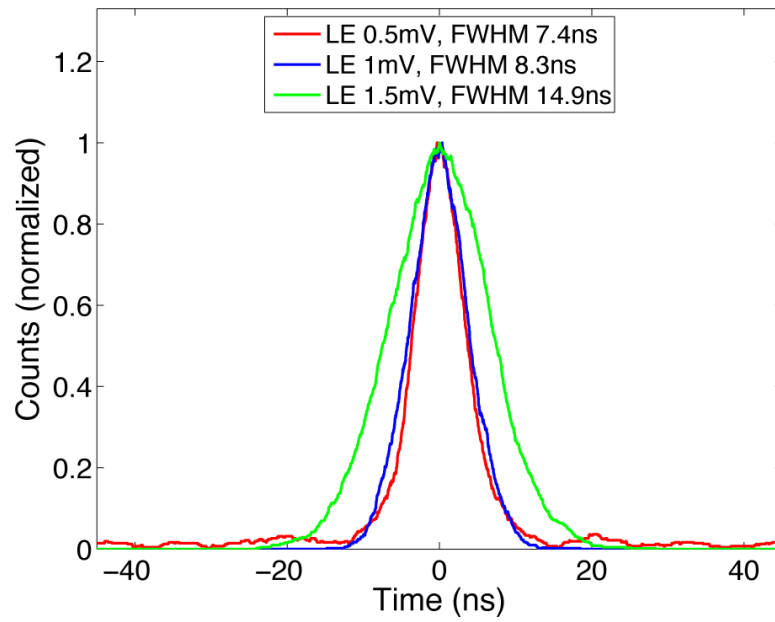A comparison of individual crystals (sizes 1.3 mm and 0.5 mm) slightly off center coupled to the 5 mm PS-SSPM. Refer to Fig. 6 and Fig. 8 for crystal locations.

Fig. 10.
Digital LE timing results, at various LE thresholds, for a single 1 mm LSO crystal coupled to the center of a 5 mm PS-SSPM. Data is from PS-SSPM vs. PS-SSPM coincidence setup; the FWHM quoted is the coincidence time resolution. No walk correction was applied.
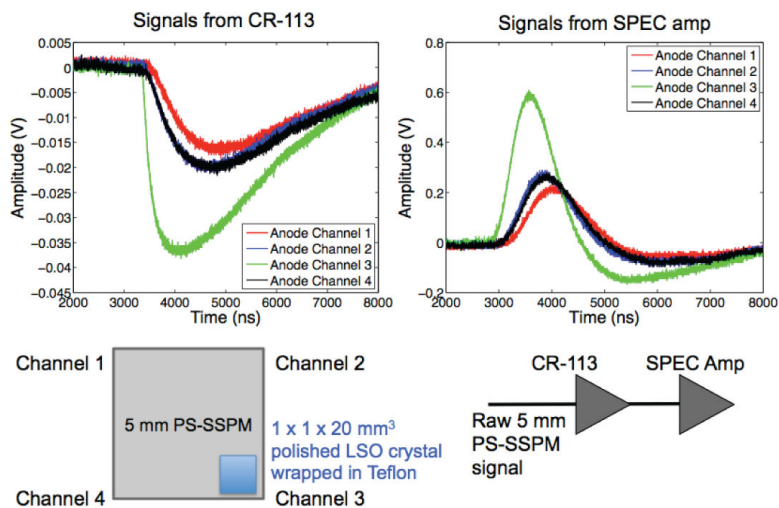
Fig. 11.
The four corner anode signals of a 5 mm PS-SSPM amplified by a CR-113 (left) and after the Caen N5678B spectroscopy amplifier (right). Note that the peak positions of each anode channel are not aligned.
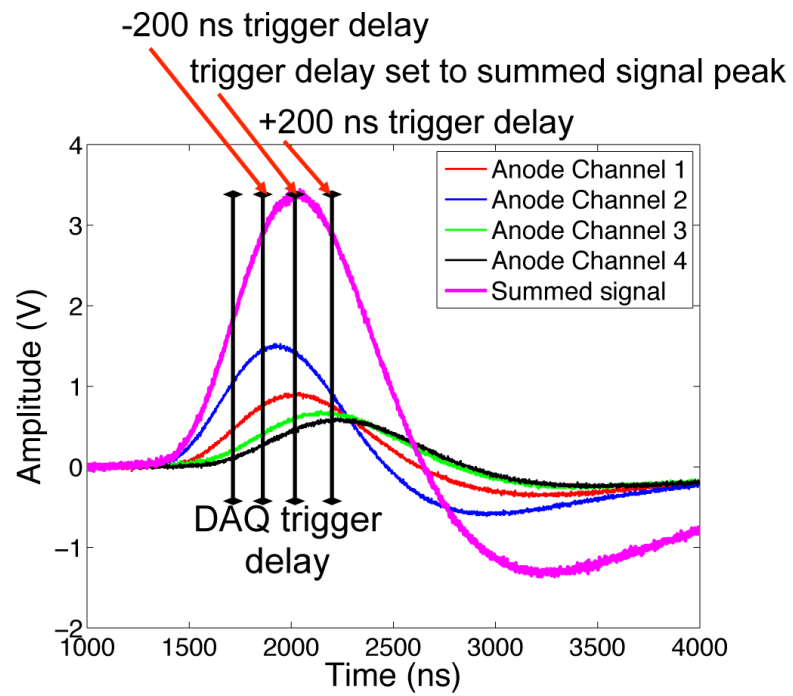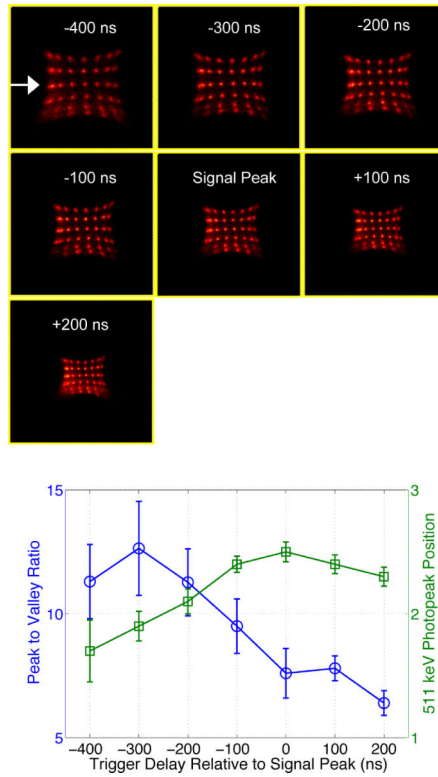
Fig. 12.
Definition of data acquisition trigger delay described in text.

Fig.13.
Top, flood histograms acquired for different DAQ trigger delays; data generated by a single ended readout of the 5 mm PS-SSPM coupled to the 0.5 mm LYSO array. Below, peak to valley ratio for the different flood histograms and 511 keV peak position (V) measured from crystals in the center of the flood histogram. The white arrow in the –400 ns flood histogram denotes the row used for the peak to valley calculation. Error bars indicate ±1σ for the peak to valley ratio and a least square error from the Gaussian fit to the 511 keV photopeak.
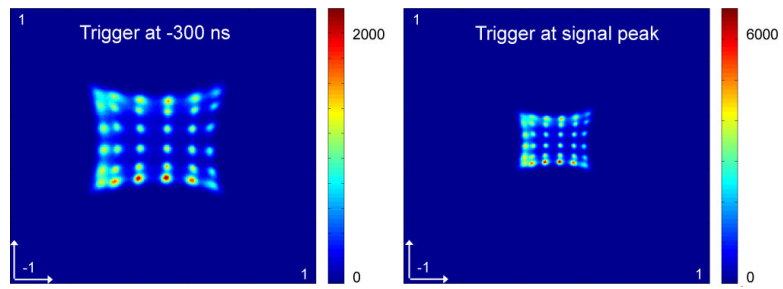
Fig. 14.
Dual-ended readout of a 0.7 mm LSO array with two 5 mm PS-SSPMs at two different trigger positions. Combined flood histograms are displayed on a 256×256 matrix.
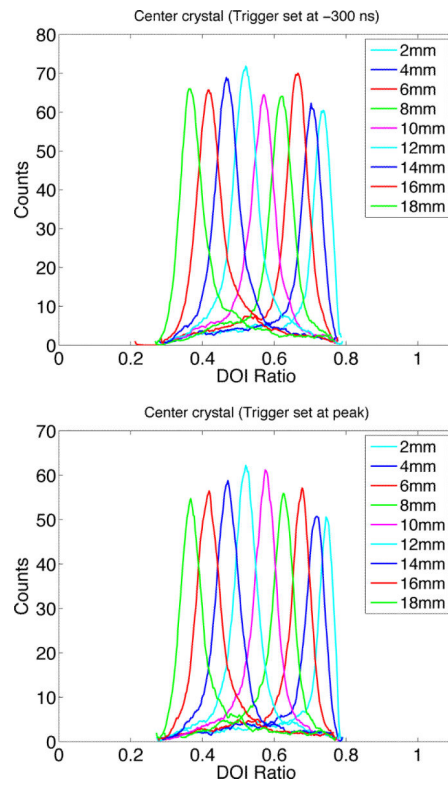
Fig. 15.
DOI response curves from a single crystal in the 0.7 mm LSO array using a dual-ended readout with 5 mm PS-SSPMs. Top: data from a trigger delay set at –300 ns. Bottom: trigger delay set at signal peak.
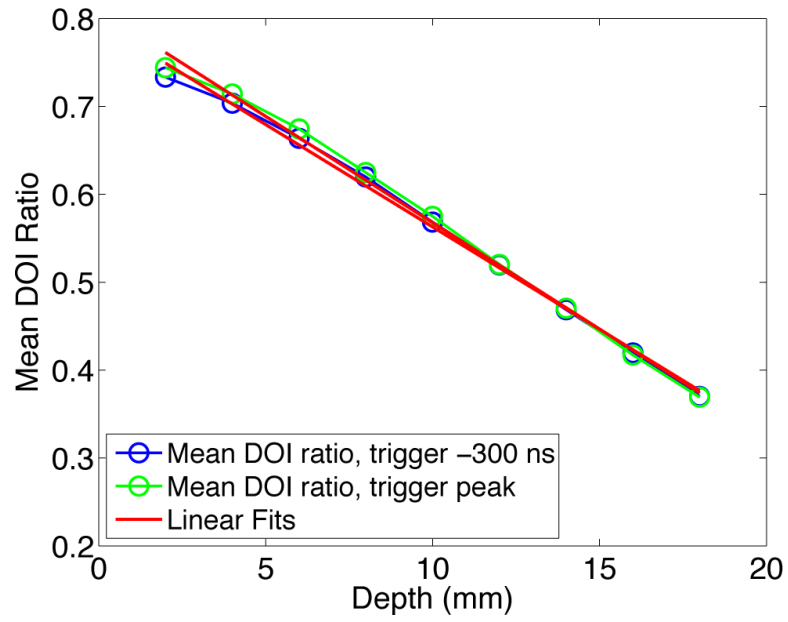
Figure 16.
DOI calibration curve used to calculate DOI resolution. The DOI ratio as a function of depth is independent of the trigger delay.
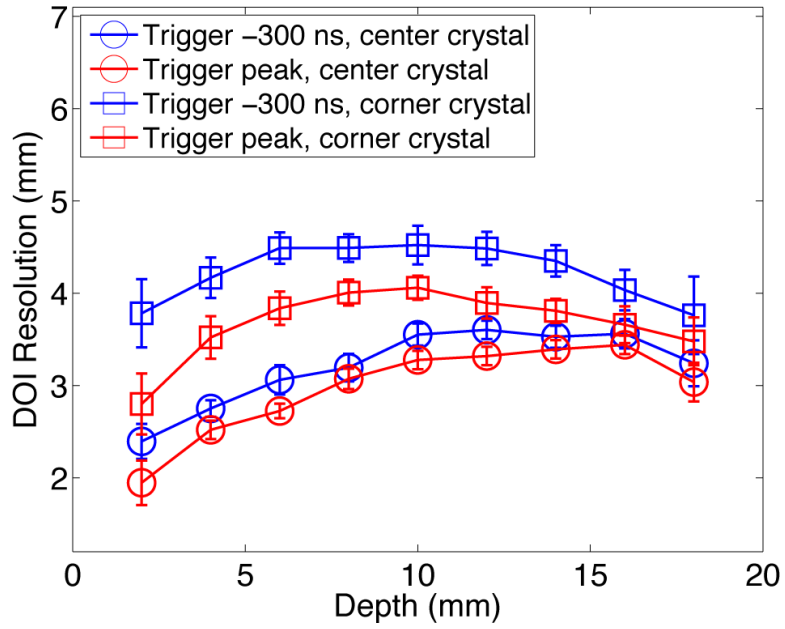
Fig. 17.
Measured DOI resolution as a function of depth using the 0.7 mm LSO array readout at both ends with 5 mm PS-SSPMs. Data is shown for center and corner crystals, using a trigger delay of –300 ns and at the signal peak. Data points represent average DOI resolution of four crystals. Four crystals in the center of the LSO array and the four corner crystals were used. Error bars indicate ±1σ for the set of DOI resolution measurements.

TABLE I

Summary of device parameters for 5 mm × 5 mm and 10 mm × 10 mm PS-SSPMs

	5 mm × 5 mm PS-SSPM	**10 mm × 10 mm PS-SSPM**
Photon Detection Efficiency @ 420 nm	~10%	~10%
Micro-Pixel Area	30 μm × 30 μm	30 μm × 30 μm
Micro-Pixel Pitch	44.3 μm × 44.3 μm	44.3 μm × 44.3 μm
Geometrical Fill Factor	0.46	0.46
Total Number of Micro-Pixels	11664 (108×108)	40000 (200×200)
Dark Count Rate (Hz)	1.21×10^8	6.18×10^8
Network Resistors (Ω)	246.5	90
Capacitance (fF/pixel)	220	220
Estimated Total Capacitance (nF)	2.6	8.8

TABLE II

Summary of detector configurations and reported measurements

	Detector Configuration	Measurement
Section II-B.1	Single ended readout of a 6 × 6 LSO array with 1.3 mm crystal size by a 5 mm PS-SSPM and a continuous 10 mm PS-SSPM	Timing properties (timing resolution and time shift) with different time pick-off methods
Section II-B.2, Section II-D	Single ended readout of 0.5 mm LYSO array with a single 5mm PS-SSPM in the 2 × 2 PS-SSPM array	Timing properties. Energy estimation and flood quality at different DAQ settings
Section II-C	Two 5 mm PS-SSPMs in coincidence using individual 1 mm crystals coupled to the device center	Timing resolution by digital methods
Section II-E	Dual ended readout of a 6 × 6 LSO array with 0.7 mm crystal size using two 5 mm PS-SSPMs	Comparison of depth of interaction resolution and flood quality at two DAQ settings

TABLE III

Block timing results, after crystal time-shift correction, with the 1.3 mm LSO array. Measurements were performed using different time-pick off methods; leading edge thesholds are given in mV and constant fraction delays in ns.

5mm × 5 mm PS-SSPM

Average timing resolution (ns) ~250 keV energy threshold

Temperature	3 mV	4 mV	5 mV	40 ns	50 ns	60 ns
0°C	13.7	14.9	16.1	12	12	12.1
20°C	13.8	15	15.5	12.4	12.4	12.4

Average timing resolution (ns) ~450 keV energy threshold

Temperature	3 mV	4 mV	5 mV	40 ns	50 ns	60 ns
0°C	8	8.1	8.2	8.5	8.5	8.5
20°C	10	9.7	9.8	9.7	9.6	9.6

10 mm × 10 mm PS-SSPM

Average timing resolution (ns) ~250 keV energy threshold

Temperature	3 mV	4 mV	5 mV	40 ns	50 ns	60 ns
0°C	11.5	10.7	10.7	10.2	10.3	10.4
20°C	13.9	13.4	13.5	12.7	12.6	12.7

Average timing resolution (ns) ~450 keV energy threshold

Temperature	3 mV	4 mV	5 mV	40 ns	50 ns	60 ns
0°C	9.4	8.9	8.8	8.6	8.6	8.7
20°C	11.9	11.7	11.8	10.9	10.9	11